frontiers | Frontiers in Chemistry

TYPE Original Research
PUBLISHED 20 October 2022
DOI 10.3389/fchem.2022.1052560

OPEN ACCESS

EDITED BY
Junhao Liu,
Institute of Process Engineering (CAS), China

REVIEWED BY
Weijia Zhou,
University of Jinan, China
Huawei Song,
Sun Yat-sen University, China

*CORRESPONDENCE
Shaonan Gu,
sngu@qlu.edu.cn
Guowei Zhou,
gwzhou@qlu.edu.cn
Jinling Chai,
jlchai@sdnu.edu.cn

SPECIALTY SECTION
This article was submitted to Electrochemistry, a section of the journal Frontiers in Chemistry

RECEIVED 24 September 2022
ACCEPTED 10 October 2022
PUBLISHED 20 October 2022

CITATION
Wang Q, Wu Y, Pan N, Yang C, Wu S, Li D, Gu S, Zhou G and Chai J (2022), Preparation of rambutan-like $Co_{0.5}Ni_{0.5}Fe_2O_4$ as anode for high−performance lithium−ion batteries. *Front. Chem.* 10:1052560. doi: 10.3389/fchem.2022.1052560

Preparation of rambutan-like $Co_{0.5}Ni_{0.5}Fe_2O_4$ as anode for high−performance lithium−ion batteries

Qian Wang[1], Yongzi Wu[2], Ning Pan[1], Chenyu Yang[2], Shuo Wu[2], Dejie Li[1], Shaonan Gu[2]*, Guowei Zhou[2]* and Jinling Chai[1]*

[1]College of Chemistry, Chemical Engineering and Materials Science, Shandong Normal University, Jinan, China, [2]Key Laboratory of Fine Chemicals in Universities of Shandong, Jinan Engineering Laboratory for Multi-scale Functional Materials, School of Chemistry and Chemical Engineering, Qilu University of Technology (Shandong Academy of Sciences), Jinan, China

$NiFe_2O_4$ is a kind of promising lithium ion battery (LIB) electrode material, but its commercial applications have been limited due to the electronic insulation property and large volume expansion during the conversion reaction process, which results in rapid capacity decrease and poor cycling stability. We synthesized rambutan-like $Co_{0.5}Ni_{0.5}Fe_2O_4$ using the self-templating solvothermal method. The special structure of $Co_{0.5}Ni_{0.5}Fe_2O_4$ which was formed by the assembly of numerous nanosheets could effectively buffer the volume change during the charging and discharging process. Partial substitution of Ni with Co. in $NiFe_2O_4$ leads to $Co_{0.5}Ni_{0.5}Fe_2O_4$, the coexisting of both nickel and cobalt components is expected to provide more abundant redox reactions. The specific capacity of the rambutan-like $Co_{0.5}Ni_{0.5}Fe_2O_4$ as an anode material for LIB could reach 963 mA h g^{-1} at the current density of 500 mA g^{-1} after 200 cycles, confirming that the as-synthesized material is a promising candidate for LIBs.

KEYWORDS

ternary metal oxides, rambutan-like nanostracture, synergetic effect, anode material, lithium-ion battery

Introduction

LIB has been widely used in portable electronic items and electric vehicles as an important electronic energy storage device (Huang et al., 2018). With the increasing demand for practical application, developing high electrochemical performance LIB electrode materials is highly desirable (Yang et al., 2017; Luo et al., 2019). Metal oxides have been the focus of recent research on LIB anode materials due to the advantages including high theoretical specific capacity, high power density, pseudo capacitance effect and practical safety (Bi et al., 2020; Lu et al., 2018a; Song et al., 2018; J. Wang et al., 2017). In particular, the transition-metal oxides with spinel structure including $MnCo_2O_4$ (Li et al., 2014), $NiCo_2O_4$ (Shen et al., 2015), and Co_3O_4 (Wang et al., 2013) have been the research hotspot of anode materials for LIBs due to the distinctive

crystal structure, synergistic reaction between metal ions, multiple oxidation states and other advantages (Jiao et al., 2019; Li J. et al., 2019; Weng et al., 2020). However, the electronic insulation performance and ion transport instability of the spinel transition metal oxides lead to the irreversible capacity and poor cycle stability of the battery, which hinder their application (Wang J. et al., 2016; Wu et al., 2017; Wu et al., 2020).

It was found that inverse spinel structured ferrites can incorporate more Li^+ than normal spinel structured ferrite (Chen and Greenblatt, 1986). As a typical inverse spinel structured ferrite, $NiFe_2O_4$ has a unique structure in which the Ni^{2+} and half of the Fe^{3+} occupies octahedral positions while the rest Fe^{3+} are distributed in tetrahedral voids (Qu et al., 2017). Therefore, during the insertion and extraction process, the structure can accommodate eight Li^+ per unit, which resulting in the high theoretical capacity of the $NiFe_2O_4$ (Islam et al., 2017; Tong et al., 2017). Nevertheless, as a promising LIB material, the commercial applications of $NiFe_2O_4$ cannot be realized because of the electronic insulation property and large volume expansion in the conversion reaction, which leads to the fast capacity decrease and poor cycling stability (Xiao et al., 2017). Up to now, many efforts have been conducted to solve this problem. One solution is to designing unique internal structures of $NiFe_2O_4$, such as hollow nanospheres (Gao et al., 2017), yolk-shell structure (Liu et al., 2020) nanofibers (Luo et al., 2014) and so on. Another promising strategy is coupling with highly conductive materials, such as graphene (Shen et al., 2021), carbon-based materials (Mujahid et al., 2019) and so on. However, these methods have some disadvantages, such as complicated preparation procedures, harsh conditions, or reducing energy densities by the coupled component (Huang et al., 2014).

Recently, doping with one or several metal ions to form ternary metal oxide by controlling morphology and composition has become one of the effective methods to modify spinel oxides. For examples, Li et al. synthesized double-shelled $Co_{0.5}Ni_{0.5}MoO_4$ hollow spheres through a facile spray drying process with further post annealing (Li L. et al., 2019), Lu et al. prepared $NiCo_2V_2O_8$ with yolk-double-shelled structure through a facile self-templating strategy (Lu et al., 2018b). Recently, our group demonstrated that the yolk–double shelled $Mn_{0.5}Zn_{0.5}Co_2O_4$/C nanospheres could obtain outstanding Li-ions storage performance (Ren et al., 2022a). The several possible redox sites, multiple oxidation states and abundant active sites in the ternary metal systems could help to increase the charge diffusion rate and ion-diffusion rate, which further improves the electronic conductivity, electrochemical activity, mechanical and chemical stability (Gonçalves et al., 2020).

Based on above researches, doping a multi-chemical valence ions, such as cobalt ions, into the lattice of inverse spinel $NiFe_2O_4$ may be an effective method to improve the lithium storage ability of $NiFe_2O_4$ through enhancing the electronic conductivity due to the synergistic effect between the several metals (Li J. et al., 2019). In addition, the combination of nickel and cobalt species is helpful to offer more abundant redox reactions (Liang et al., 2014; Guan et al., 2017). Furthermore, we synthesized rambutan-like $Co_{0.5}Ni_{0.5}Fe_2O_4$ using the self-templating solvothermal method. The special structure of $Co_{0.5}Ni_{0.5}Fe_2O_4$ which was formed by the assembly of numerous nanosheets could effectively buffer the volume change during the charging and discharging process. Partial substitution of Ni with Co. in $NiFe_2O_4$ leads to $Co_{0.5}Ni_{0.5}Fe_2O_4$, which is a promising material that integrates the high capacity of $NiFe_2O_4$ and the cycling stability of $CoFe_2O_4$ (Li L. et al., 2019). The specific capacity of the rambutan-like $Co_{0.5}Ni_{0.5}Fe_2O_4$ as a LIB anode material could reach 963 mA h g^{-1} at the current density of 500 mA g^{-1} after 200 cycles, confirming the as-synthesized material is a potential candidate for LIBs.

Experimental section

Chemicals

$Fe(NO_3)_3{\cdot}9H_2O$, $Ni(NO_3)_2{\cdot}6H_2O$ and $Co.(NO_3)_2{\cdot}6H_2O$ were purchased from Sigma-Aldrich. Isopropyl alcohol, glycerol and ethanol were purchased from Sinopharm Chemical Reagent Co., Ltd. All purchased chemicals were directly used. Ultrapure water used throughout the experiments was obtained from a MilliQ water purification system.

Synthesis of $Co_{0.5}Ni_{0.5}Fe_2O_4$

Firstly, 0.101 g of $Fe(NO_3)_3{\cdot}9H_2O$, 0.0182 g of $Co.(NO_3)_2{\cdot}6H_2O$ and 0.0183 g of $Ni(NO_3)_2{\cdot}6H_2O$ were added to 48 ml mixed solvents of glycerol and isopropanol (1:5 by volume) under stirring. The formed orange-yellow clear solution was poured into a 100 ml Teflon container, then heated to 180°C and reacted for 6 h. The product was washed by centrifugation with ethanol and then dried at 60°C. Finally, the obtained yellow precipitate was annealed at 400°C in air for 2 h to form $Co_{0.5}Ni_{0.5}Fe_2O_4$ nanospheres. The $NiFe_2O_4$ and $CoFe_2O_4$ were synthesized through the same method.

Structural characterization

X-ray diffraction (XRD) patterns were obtained using a Bruker D8-ADVANCE (40 kV, 40 mA) diffractometer. The morphology and structure of the products were observed using field emission electron microscope (FESEM, Hitachi S-4800) and high resolution transmission electron microscope (HRTEM, JEM-2100). The elemental valence was analyzed through X-ray photoelectron spectroscope which was collected

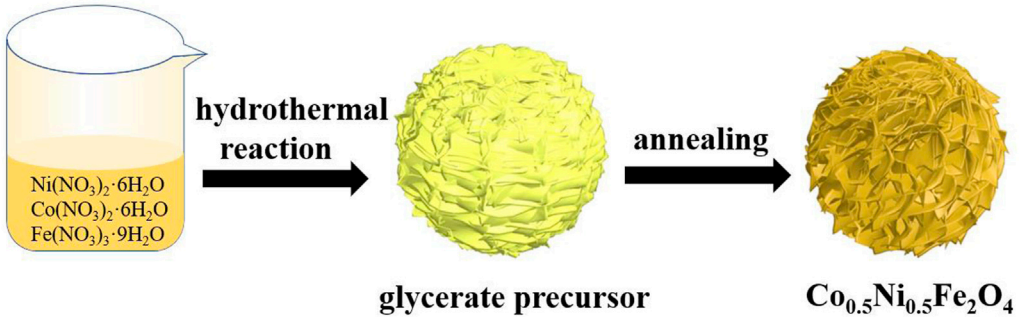

SCHEME 1
Schematic diagram of the preparation process of $Co_{0.5}Ni_{0.5}Fe_2O_4$ nanospheres.

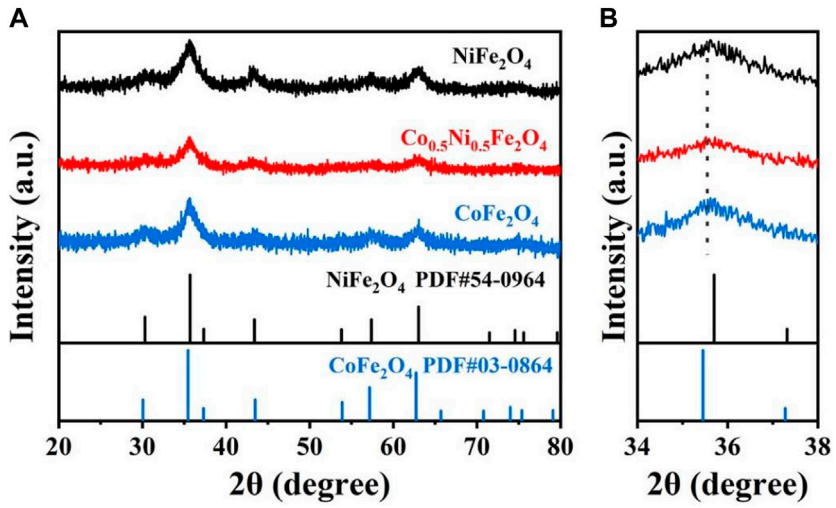

FIGURE 1
(A) XRD patterns of the obtained $Co_{0.5}Ni_{0.5}Fe_2O_4$, $NiFe_2O_4$ and $CoFe_2O_4$. **(B)** XRD comparison of $Co_{0.5}Ni_{0.5}Fe_2O_4$, $NiFe_2O_4$ and $CoFe_2O_4$ at 34°–38° after magnification.

by the X-ray energy spectrometer (ESCALAB MKII). The surface area and porosity analyzer (ASAP 2020 HD88) was used to analyze the specific surface area and pore size distribution. The accurate content of Co., Ni and Fe was analyzed by ICP-MS (NexION 350X).

Electrodes fabrication and electrochemical measurements

The prepared samples, acetylene black, and sodium carboxymethyl cellulose (CMC, 10 wt%) are mixed together with the mass ratio of 7:2:1. After adding solvent deionized water, the mixture was uniformly ground for 3 h using a planetary ball mill, then coated on the Cu foil. The coated Cu foil was cut into circular slices with the radius of 6 mm after drying in vacuum, and each with the area loading of about 1.5 mg cm^{-2}. In a glovebox filled with argon, coin cell was prepared using the Celgard 2,400 as separator, and the lithium metal foil as counter electrode. The electrolyte is 40 µl of 1.0 mol L^{-1} $LiPF_6$ dissolved in a 1:1:1 volume ratio of EC, DMC, and EMC. The LAND electrochemical station was used to test the cycling performance and rate capability of the cells. The PARSTAT 4000 electrochemical workstation was used to collect Cyclic voltammogram (CV) and electrochemical impedance spectra (EIS).

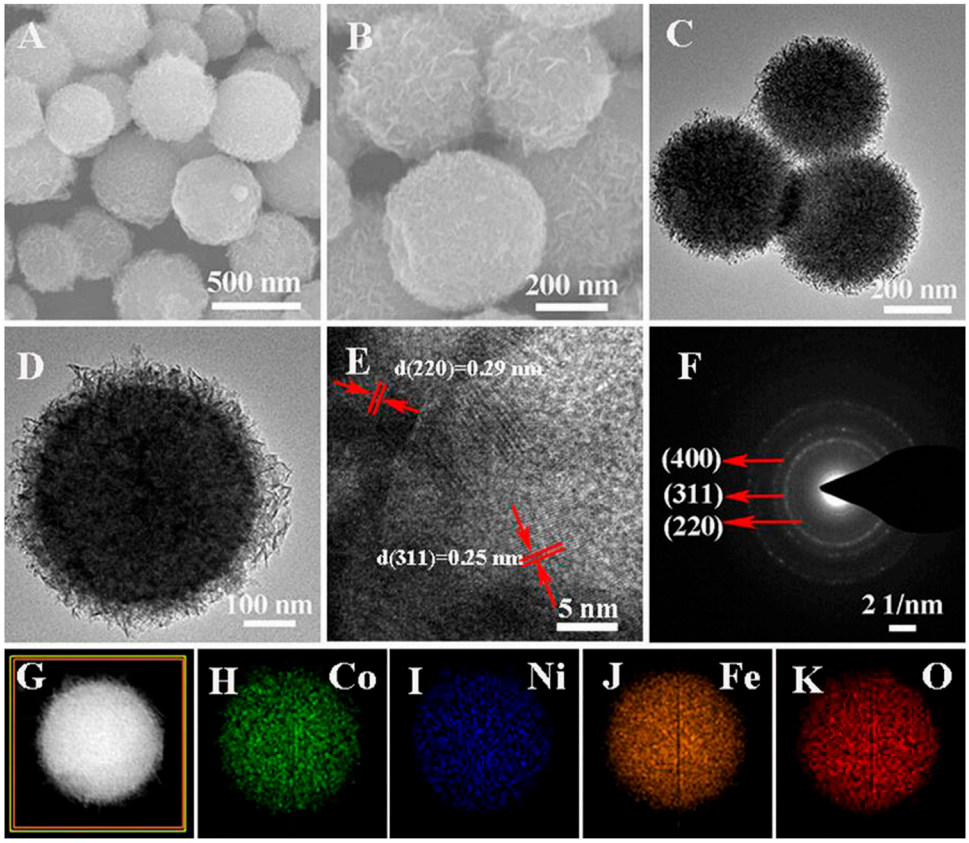

FIGURE 2
(A–B) SEM images of $Co_{0.5}Ni_{0.5}Fe_2O_4$ **(C–D)** TEM images of $Co_{0.5}Ni_{0.5}Fe_2O_4$; **(E)** HRTEM images of $Co_{0.5}Ni_{0.5}Fe_2O_4$ **(F)** SAED patterns of $Co_{0.5}Ni_{0.5}Fe_2O_4$; **(G–K)** EDX element mappings of $Co_{0.5}Ni_{0.5}Fe_2O_4$.

Results and discussion

The strategy and mechanism for preparing $Co_{0.5}Ni_{0.5}Fe_2O_4$ nanospheres is illustrated in Scheme 1. Firstly, CoNiFe-glycerate was prepared through the solvothermal method. The Ni^{2+}, Co^{2+} and Fe^{3+} precipitated as Co-Ni-Fe hydroxides with the OH^- released by the redox reaction of isopropanol and NO^{3-}, resulting in the formation of uniform CoNiFe-glycerate nanospheres (Supplementary Figure S1). The rambutan-like structure was gradually formed in the process of solvent heat treatment due to the dehydration condensation reaction of the hydroxyl groups in glycerol at high temperature. Lastly, the CoNiFe-glycerate nanospheres transformed into $Co_{0.5}Ni_{0.5}Fe_2O_4$ nanospheres through simple heat treatment.

Figure 1A shows XRD patterns of the synthesized $Co_{0.5}Ni_{0.5}Fe_2O_4$, $NiFe_2O_4$ and $CoFe_2O_4$ materials. The synthesized $NiFe_2O_4$ and $CoFe_2O_4$ corresponded to $NiFe_2O_4$ (JCPDS No. 54-0964) and $CoFe_2O_4$ (JCPDS No. 03-0864), respectively. The characteristic peak of $Co_{0.5}Ni_{0.5}Fe_2O_4$ was quite similar to $NiFe_2O_4$ and $CoFe_2O_4$ without extra lines representing the $Co_{0.5}Ni_{0.5}Fe_2O_4$ has a single-phase and shares the same structure with both $NiFe_2O_4$ and $CoFe_2O_4$. The characteristic (311) plane at 2θ of 35.5 also indicating the spinel structure of $Co_{0.5}Ni_{0.5}Fe_2O_4$ sample (Shehnaz et al., 2021). The slight peak shift can be observed in Figure 1B, and the characteristic peak of $Co_{0.5}Ni_{0.5}Fe_2O_4$ was found between $NiFe_2O_4$ and $CoFe_2O_4$. Indirectly, the successful fabrication of the ternary metal oxide $Co_{0.5}Ni_{0.5}Fe_2O_4$ was demonstrated. The shift of peak position implying the expansion of lattice volume which is attributed to the different ionic radii of Ni^{2+} (0.69 Å) and Co^{2+} (0.74 Å) ions (Chen et al., 2015).

The SEM images (Figures 2A,B) show that the $Co_{0.5}Ni_{0.5}Fe_2O_4$ were highly uniform spheres of about 500 nm in size. As shown in Figures 2C,D, the $Co_{0.5}Ni_{0.5}Fe_2O_4$ possessed a rambutan-like structure. The SEM and TEM images of $NiFe_2O_4$ and $CoFe_2O_4$ were shown in Supplementary Figure S1, both the $NiFe_2O_4$ and $CoFe_2O_4$ were highly uniform spheres of about 500 nm in size, which were similar to the $Co_{0.5}Ni_{0.5}Fe_2O_4$. Figure 2E shows the HRTEM image of a single $Co_{0.5}Ni_{0.5}Fe_2O_4$, the lattice spacings of 0.25, 0.29 and 0.48 nm identical to (311) (220) and (111) d-spacing of $Co_{0.5}Ni_{0.5}Fe_2O_4$, respectively. Meanwhile, three corresponding rings in the crystal

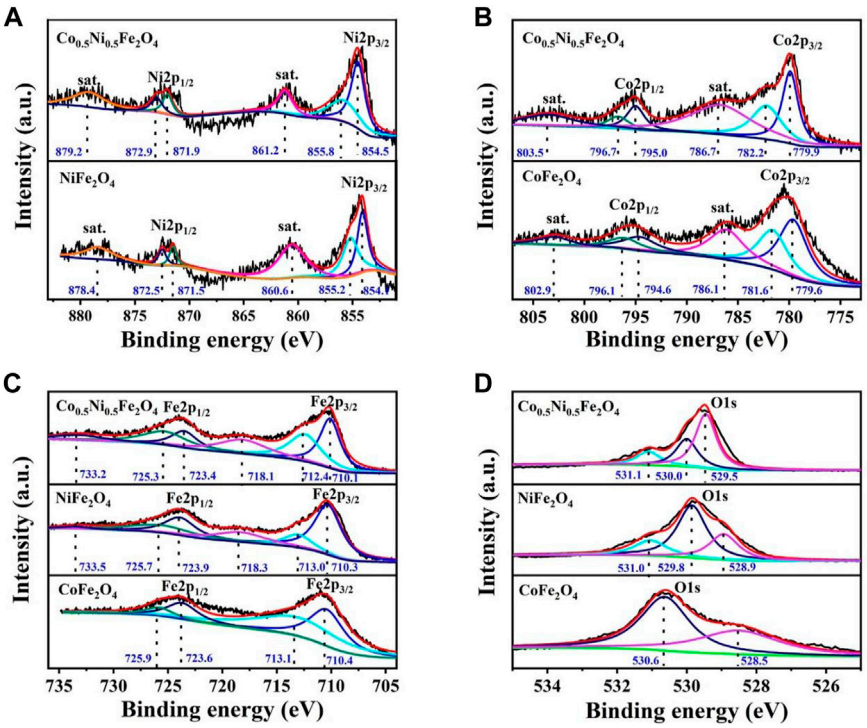

FIGURE 3
XPS spectra of the $Co_{0.5}Ni_{0.5}Fe_2O_4$, $NiFe_2O_4$ and $CoFe_2O_4$ spheres **(A)** Ni 2p; **(B)** Co. 2p **(C)** Fe 2p; and **(D)** O1s.

plane were observed clearly in the selected area electron diffraction (SAED) image (Figure 2F) indicating that the crystallinity of the $Co_{0.5}Ni_{0.5}Fe_2O_4$ is good. In addition, the EDS element mapping images of Co., Ni, Fe, O (Figures 2G–K) indicating the homogeneous distribution of these elements in $Co_{0.5}Ni_{0.5}Fe_2O_4$ and further indicating the single-phase property of the obtained products. To confirm the chemical composition of the $Co_{0.5}Ni_{0.5}Fe_2O_4$, the Co./Ni value was identified by ICP–MS, which was nearly 1.15:1, approach to the feeding ratio (1: 1).

To further illustrate the chemical composition of $Co_{0.5}Ni_{0.5}Fe_2O_4$, XPS characterizations were employed to analyze the valence states of each element in the $Co_{0.5}Ni_{0.5}Fe_2O_4$, $NiFe_2O_4$ and $CoFe_2O_4$ spheres, respectively. Figure 3A shows the Ni 2 p spectrum, the characteristic peaks centered at 854.5 and 871.9 eV are attributed to Ni^{2+} species while the peaks located at 855.8 and 872.9 eV represent the Ni^{3+} ion. Compared with $NiFe_2O_4$, the peak location of $Co_{0.5}Ni_{0.5}Fe_2O_4$ moved 0.4–0.8 eV to high binding energy, which attributed to the charge transfer as well as the strong interaction of the Ni–O bond. The Co_{2p} peaks at about 779.9 and 795.0 eV (Figure 3B) are attributed to Co^{2+} and the peaks at 782.2 and 796.7 eV indicating the presence of Co^{3+}, which is the result of the partial oxidation of Co^{2+} from the surface (Shehnaz et al., 2021). Meanwhile, because of the strong Co–O interaction, the binding energy of $Co_{0.5}Ni_{0.5}Fe_2O_4$ increased 0.3–0.6 eV than that of $CoFe_2O_4$. The $2p_{3/2}$ peaks at about 710.1and 712.4 eV (Figure 3C), along with the $2p_{1/2}$ peaks at around 723.4 and 725.3 eV represents the coexist of both the tetrahedral site and octahedral sites Fe^{3+} species. The satellite peaks at around 718.1 eV and 733.2 eV, also represent the presence of Fe^{3+} cations (Shehnaz et al., 2021). Compared to $NiFe_2O_4$ and $CoFe_2O_4$, the binding energy of Ni 2 p and Co. 2 p in $Co_{0.5}Ni_{0.5}Fe_2O_4$ were increased while that of Fe 2 p were decreased, which means the electrons transfer from Ni and Co. to Fe. The shift of the binding energy further demonstrated the prepared $Co_{0.5}Ni_{0.5}Fe_2O_4$ was ternary metal oxide. The characteristic peaks of $Co_{0.5}Ni_{0.5}Fe_2O_4$ at 529.5, 529.8 and 531.0 eV (Figure 3D) indicating the metal oxygen, oxygen vacancy and adsorption oxygen, respectively. The binding energy of the oxygen vacancy for $Co_{0.5}Ni_{0.5}Fe_2O_4$, $NiFe_2O_4$ and $CoFe_2O_4$ were 530.0, 529.8 and 530.6 eV (Kang et al., 2019; Pramanik et al., 2020; Ren et al., 2022b), respectively. The binding energy of O1s changes obviously with the doping of Co., indicating the successfully synthesized of $Co_{0.5}Ni_{0.5}Fe_2O_4$.

The nitrogen adsorption-desorption experiment was conducted to test the specific surface area and pore size distribution of the three samples. As can be seen in Supplementary Figure S2, all three samples have obvious hysteresis loops, indicating they are all mesoporous structure

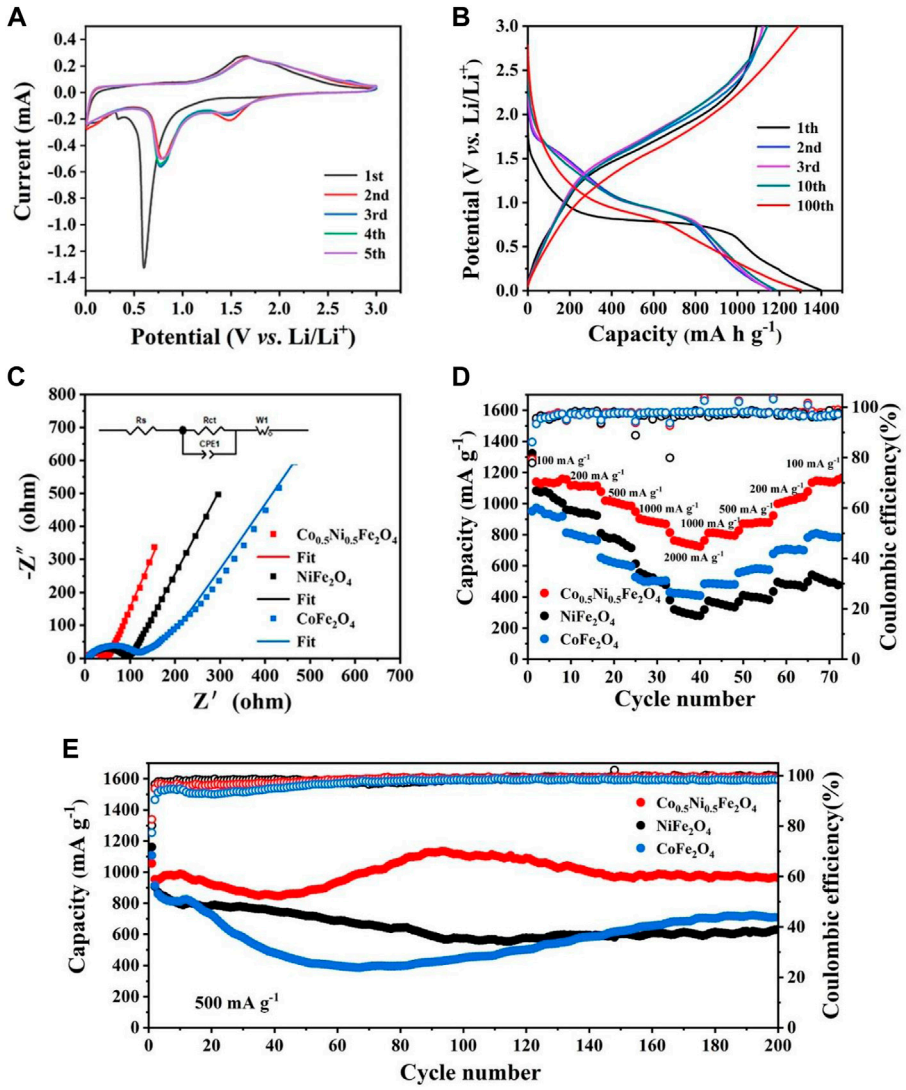

FIGURE 4
(A) CV curves of $Co_{0.5}Ni_{0.5}Fe_2O_4$ in the first five cycles at 0.1 mV s^{-1}. **(B)** Discharge-charge curves of $Co_{0.5}Ni_{0.5}Fe_2O_4$ at 200 mA g^{-1}. **(C)** Nyquist plots of the $Co_{0.5}Ni_{0.5}Fe_2O_4$, $NiFe_2O_4$ and $CoFe_2O_4$. **(D)** Rate capability of $Co_{0.5}Ni_{0.5}Fe_2O_4$, $NiFe_2O_4$ and $CoFe_2O_4$. **(E)** Cycling performance and the corresponding Coulombic efficiencies of $Co_{0.5}Ni_{0.5}Fe_2O_4$, $NiFe_2O_4$ and $CoFe_2O_4$ at 500 mA g^{-1}.

(Zhou et al., 2017). According to the analyzed results, the BET surface areas were 242.63, 177.43 and 146.84 $m^2 g^{-1}$ for $Co_{0.5}Ni_{0.5}Fe_2O_4$, $NiFe_2O_4$ and $CoFe_2O_4$, while the corresponding average diameter were 3.1, 3.2 and 4.05 nm, respectively. The higher specific surface area of $Co_{0.5}Ni_{0.5}Fe_2O_4$ is attributed to the greater surface roughness than $NiFe_2O_4$ and $CoFe_2O_4$ spheres which can be seen from the TEM and SEM images. Because of the larger BET surface area and smaller average pore size, the $Co_{0.5}Ni_{0.5}Fe_2O_4$ can offer more active sites, shorten the Li^+ transport path, and help to the reduction of polarization in the process of charge and discharge (Qu et al., 2017).

Figure 4A shows the CV curves of $Co_{0.5}Ni_{0.5}Fe_2O_4$ at 0.1 mV s^{-1} between 0.01 and 3.00 V. In the first cycle, two cathodic peaks at around 0.3 and 0.6 V were attributed to the reduction of Co., Ni and Fe in $Co_{0.5}Ni_{0.5}Fe_2O_4$ (Eq. 1) with the simultaneous formation of both Li_2O and SEI layer, one anode peak located at 1.6 V was corresponded to the oxidation of Ni, Co., and Fe (Ding et al., 2013). The cathodic peak shifted from 0.6 to about 0.8 V in the following four cycles, with a new peak appears around 1.5 V simultaneously which indicating the reversible reduction of Fe_2O_3 and MeO, respectively (Xia et al., 2021). The anode peak at 1.6 V moved to 1.7 V which was caused by the polarization of the battery (Xiao et al., 2017).

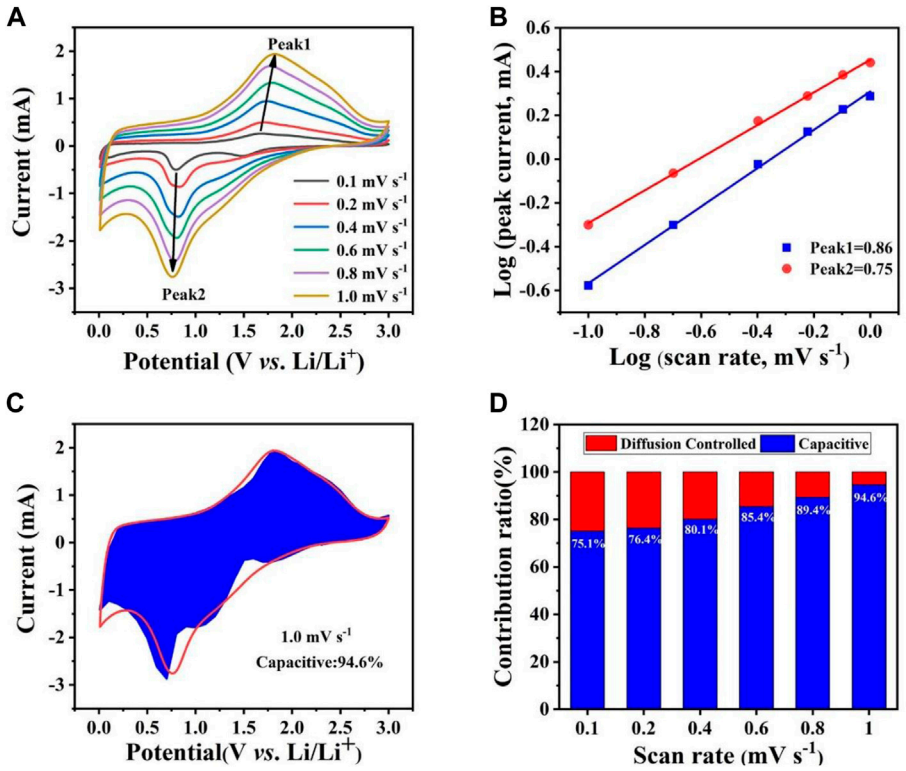

FIGURE 5
(A) CV curves of $Co_{0.5}Ni_{0.5}Fe_2O_4$ at various scan rates ranging from 0.1 mV s^{-1} to 1.0 mV s^{-1}. **(B)** the relationship between log(i) and log(*v*). **(C)** The capacitive contribution of $Co_{0.5}Ni_{0.5}Fe_2O_4$ at 1.0 mV s^{-1}. **(D)** Pseudocapacitive contribution of $Co_{0.5}Ni_{0.5}Fe_2O_4$ at different scan rates.

The electrode reaction of $Co_{0.5}Ni_{0.5}Fe_2O_4$ can be expressed by the following equation:

$$2Co_{0.5}Ni_{0.5}Fe_2O_4 + 16e^- + 16Li^+ \rightarrow Co + Ni + 4Fe + 8Li_2O \quad (1)$$

$$Ni + Li_2O \rightarrow NiO + 2Li^+ + 2e^- \quad (2)$$

$$Co + Li_2O \rightarrow CoO + 2Li^+ + 2e^- \quad (3)$$

$$2Fe + 3Li_2O \rightarrow Fe_2O_3 + 6Li^+ + 6e^- \quad (4)$$

The nearly overlapped CV curves and characteristic peaks after the first cycle, implying the electrode had satisfied reversibility and cyclic stability during discharge and charge process (Zhang et al., 2019a). The cyclic voltammograms of $NiFe_2O_4$ and $CoFe_2O_4$ are shown in Supplementary Figure S3A and S4A, and the similar profiles illustrating they have approximate lithium storage mechanism with $Co_{0.5}Ni_{0.5}Fe_2O_4$. The CV curves of the three samples were slightly different, which was attributed to their different chemical compositions. The charge-discharge curve at 200 mA g^{-1} between 0.01 and 3 V is shown in Figure 4B. The discharge plateau of the first cycle was around 0.6 V and increased to 0.8 V subsequently due to the irreversible reaction, which are identical to the CV curve. The initial discharge and charge capacity of $Co_{0.5}Ni_{0.5}Fe_2O_4$ are 1397.17 and 1092.01 mA h g^{-1}, respectively. The initial Coulombic efficiency (CE) is 78.16%, and the capacity loss of 21.84% is ascribed to the irreversible reaction and SEI film decomposition (Zhang et al., 2019b; Zou et al., 2020). Due to the activation of the electrode, the discharge capacity of the $Co_{0.5}Ni_{0.5}Fe_2O_4$ electrode decreased at the early stage, but surprisingly, the specific capacity could maintain at 1304.5 mA h g^{-1} after 100 cycles, which is obviously higher than those of $NiFe_2O_4$ (644 mA h g^{-1}) and $CoFe_2O_4$ (738 mA h g^{-1}) as shown in Supplementary Figure S5.

Electrochemical impedance spectroscope (EIS) was performed to testing the ability of electrode materials participating in the chemical reaction. The semicircle of the Nyquist diagram in the high frequency region represents charge transfer impedance (R_{ct}) on the interface of electrode and electrolyte, and the sloped line of Nyquist diagram in the low frequency region correspond to ion diffusion resistance in the electrodes (Gong et al., 2018). Figure 4C shows the Nyquist plots of $Co_{0.5}Ni_{0.5}Fe_2O_4$, $NiFe_2O_4$ and $CoFe_2O_4$. According to the fitting results, the R_{ct} of $Co_{0.5}Ni_{0.5}Fe_2O_4$ was about 36.6 Ω while the values of $NiFe_2O_4$ and $CoFe_2O_4$ were 77.7 and 86 Ω, respectively. The EIS spectrum of $Co_{0.5}Ni_{0.5}Fe_2O_4$ also exhibits larger slope than those of $NiFe_2O_4$ and $CoFe_2O_4$ in the low frequency regime. The EIS results shows that $Co_{0.5}Ni_{0.5}Fe_2O_4$ anode material has lower resistance, which is contributed to the transfer of electron and Li^+, resulting in the improved electrochemical performance.

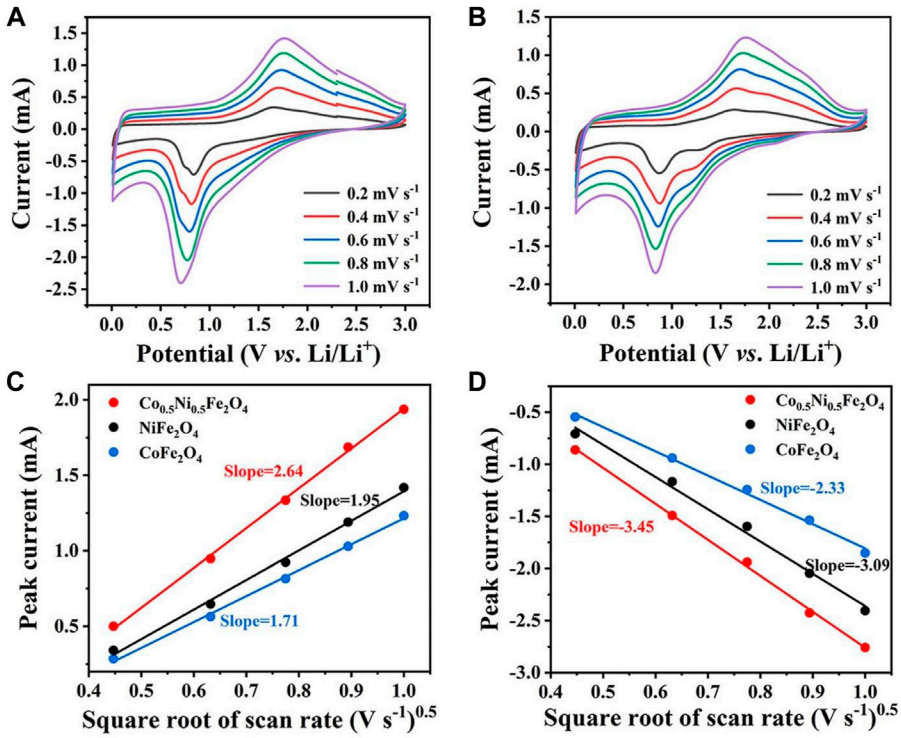

FIGURE 6
CV curves of **(A)** $NiFe_2O_4$ and **(B)** $CoFe_2O_4$ at various scan rates. Linear relationship between CV peak current of **(C)** anodic and **(D)** cathodic peaks and the square root of scan rate for $NiFe_2O_4$ and $CoFe_2O_4$, and $Co_{0.5}Ni_{0.5}Fe_2O_4$.

Figure 4D depicts the rate capability of the three electrode materials. When the current density was up to 2000 mA g^{-1}, the capacity of $Co_{0.5}Ni_{0.5}Fe_2O_4$ can reach 763 mA h g^{-1}. As the current density gradually returned to 100 mA g^{-1}, the specific capacity of $Co_{0.5}Ni_{0.5}Fe_2O_4$ increased to 1154 mA h g^{-1} while the corresponding CE maintained at around 98.9%. This result indicated that the cycling stability of $Co_{0.5}Ni_{0.5}Fe_2O_4$ is very well. However, as the current density decreased gradually, the specific capacity of $NiFe_2O_4$ did not increase obviously, indicating its cyclic stability was poor. Although the capacity of $CoFe_2O_4$ increased as the current density decreased, the capacity only reached 785 mA h g^{-1} at 100 mA g^{-1}. The results indicating that the $Co_{0.5}Ni_{0.5}Fe_2O_4$ has significantly higher specific capacity and stability than $NiFe_2O_4$ and $CoFe_2O_4$.

Figure 4F shows the results of cyclic stability of the samples at 500 mA g^{-1} for 200 cycles. The specific capacity of $NiFe_2O_4$ gradually decreased during the initial 90 cycles, then maintained at about 631.5 mA h g^{-1} as the number of cycles increases. During the first 60 cycles, the specific capacity of $CoFe_2O_4$ decreased to 400 mA h g^{-1}, and then increased to 708.5 mA h g^{-1} after 200 cycles. In contrast, the capacity of $Co_{0.5}Ni_{0.5}Fe_2O_4$ has a slightly decrease in the first 40 cycles, then gradually increases and finally stabilizes at about 963 mA h g^{-1} after 200 cycles. The specific capacity of the $Co_{0.5}Ni_{0.5}Fe_2O_4$ electrode increases with the number of cycles, and then slightly decreases with the fluctuation, which might be originated from the much slower and more sufficient activation of the fresh electrode, as well as the decreased side reactions in the electrode/electrolyte interface after the formation of SEI (Wang Z. et al., 2016; Gao et al., 2017). In addition, the increase in specific capacity may be related to factors such as activation and adequate infiltration of the electrolyte, as depicted and described in many other publications (Xu et al., 2020; Zhang et al., 2020). The initial Coulombic Efficiency (CE) of $Co_{0.5}Ni_{0.5}Fe_2O_4$ electrode was 82.7% at the current density of 500 mA g^{-1}. The long cycle curves of samples at the current densities of 200 and 1000 mA g^{-1} are shown in Supplementary Figure S6. When cycled at the current densities of 200 and 1000 mA g^{-1}, the initial CEs of the $Co_{0.5}Ni_{0.5}Fe_2O_4$ electrodes were determined to be 78.2% and 79.3%, respectively. The capacity of $Co_{0.5}Ni_{0.5}Fe_2O_4$ can stabilized at 1190 mA h g^{-1} after 200 cycles at 200 mA g^{-1}. When the current density reached 1000 mA g^{-1}, the specific capacity of both the $NiFe_2O_4$ and $CoFe_2O_4$ decreased rapidly and finally stabilized at about 400 mA h g^{-1}. However, the capacity of $Co_{0.5}Ni_{0.5}Fe_2O_4$ has a slightly decrease in the first 60 cycles at 1000 mA g^{-1}, then increased gradually and tend to be stable, finally stabilized at about 850 mA h g^{-1} after 200 cycles. This result demonstrated the superior electrochemical stability of the $Co_{0.5}Ni_{0.5}Fe_2O_4$.

The CV test was performed (Figure 5A) to further explore the lithium storage mechanism of the $Co_{0.5}Ni_{0.5}Fe_2O_4$, which can be calculated using the equation:

$$\log(i) = b\log(v) + \log(a) \quad (5)$$

Generally, when $b = 0.5$, the electrochemical process contributes by diffusion whereas the capacitive effect will play the dominate role when the value of b is up to 1.0 (Jiang and Liu, 2019; Acharya et al., 2021). As shown in Figure 5B, the values of b shown by peak one and peak two were 0.75 and 0.86, respectively. This result suggests that the pseudo capacitive effect is the main factor driving the electrochemical process. Figures 5C,D demonstrate that the contribution of the capacitive effect gradually becomes higher as scan rates increase. The contribution of pseudo capacitive for the $Co_{0.5}Ni_{0.5}Fe_2O_4$ anode reached 94.6% at the scan sweep rate of 1.0 mV s^{-1} while those of the $NiFe_2O_4$ and $CoFe_2O_4$ were 92.0% (Supplementary Figure S3C) and 91.7% (Supplementary Figure S4C), respectively. The result shows that the $Co_{0.5}Ni_{0.5}Fe_2O_4$ material with higher capacitance contribution can provide more active sites and transmission routes, further improve the electrochemical cycling performance.

The CV curves of $NiFe_2O_4$ and $CoFe_2O_4$ at different scan rates are shown in Figures 6A,B. The Randles-Sevcik equation can be used to calculate the diffusion coefficient of Li^+:

$$I_p = 2.69 \times 10^5 n^{3/2} A D_{Li}^{1/2} v^{1/2} \Delta C_0 \quad (6)$$

I_p refers to the peak current of the CV curves, A represents the electrode area, n means the number of electron transfer, v is the scan rate, D refer to the Li^+ diffusion coefficient, and C_0 is the concentration of electrolyte. Since A, n, v, and ΔC_0 are all constants in this equation, the slope of the curve can represent the Li^+-diffusion capability (Wang et al., 2020; Ren et al., 2022a). As shown in Figures 6C,D, the slope of the curve for $Co_{0.5}Ni_{0.5}Fe_2O_4$ was obviously higher than those of $NiFe_2O_4$ and $CoFe_2O_4$, indicating that the $Co_{0.5}Ni_{0.5}Fe_2O_4$ has the largest Li^+ diffusion coefficient which further proved that the rambutan-like sphere with a high surface area was more helpful to the Li^+ transport.

Conclusion

In conclusion, we synthesized the rambutan-like ternary metal oxide $Co_{0.5}Ni_{0.5}Fe_2O_4$ by a facile self-templating solvothermal method. The special structure and large specific surface area of the sample can effectively buffer the volume changes and offer more active sites during the Li^+ insertion and extraction processes. Due to the synergistic interaction between metal ions, the anode can still maintain a high specific capacity after 200 cycles at the current density of 500 mA g^{-1}, indicating the electrode material has strong lithium storage performance. The work shows that the electrochemical performance can be improved through designing unique components and structures of the anode materials. Furthermore, this method can be expanded to prepare additional metal oxide for the fabrication of potential anodes for LIBs.

Data availability statement

The original contributions presented in the study are included in the article/Supplementary Material, further inquiries can be directed to the corresponding authors.

Author contributions

QW, Methodology, formal analysis, writing-original draft. YW, Investigation, methodology. NP, Methodology, formal analysis. CY, Investigation, methodology, formal analysis. SW, Visualization, verification. DL, Methodology, formal analysis. SG, Writing-review and editing, formal analysis, funding acquisition, supervision. GZ, Writing-review and editing, funding acquisition, supervision. JC, Writing-review and editing, funding acquisition, supervision.

Funding

This work was supported by the National Natural Science Foundation of China (Grant Nos. 22108133, 51972180), the Program for Scientific Research Innovation Team in Colleges and Universities of Jinan (Grant No. 2018GXRC006) and the Shandong Provincial Natural Science Foundation, China (No. ZR2020MB038).

Conflict of interest

The authors declare that the research was conducted in the absence of any commercial or financial relationships that could be construed as a potential conflict of interest.

Publisher's note

Supplementary material

The Supplementary Material for this article can be found online at: https://www.frontiersin.org/articles/10.3389/fchem.2022.1052560/full#supplementary-material

References

Acharya, J., Ojha, G. P., Kim, B. S., Pant, B., and Park, M. (2021). Modish designation of hollow-tubular rGO-NiMoO4@Ni-Co-S hybrid core-shell electrodes with multichannel superconductive pathways for high-performance asymmetric supercapacitors. *ACS Appl. Mat. Interfaces* 13 (15), 17487–17500. doi:10.1021/acsami.1c00137

Bi, R., Xu, N., Ren, H., Yang, N., Sun, Y., Cao, A., et al. (2020). A hollow multi-shelled structure for charge transport and active sites in lithium-ion capacitors. *Angew. Chem. Int. Ed.* 59 (12), 4865–4868. doi:10.1002/anie.201914680

Chen, C. J., Greenblatt, M., and Waszczak, J. (1986). Lithium insertion into spinel ferrites. *Solid State Ionics* 18 (19), 838–846. doi:10.1016/0167-2738(86)90273-0

Chen, H., Chen, S., Fan, M., Li, C., Chen, D., Tian, G., et al. (2015). Bimetallic nickel cobalt selenides: A new kind of electroactive material for high-power energy storage. *J. Mat. Chem. A* 3 (47), 23653–23659. doi:10.1039/c5ta08366d

Ding, Y., Yang, Y., and Shao, H. (2013). One-pot synthesis of NiFe2O4/C composite as an anode material for lithium-ion batteries. *J. Power Sources* 244, 610–613. doi:10.1016/j.jpowsour.2013.01.043

Gao, X., Wang, J., Zhang, D., Nie, K., Ma, Y., Zhong, J., et al. (2017). Hollow NiFe2O4 nanospheres on carbon nanorods as a highly efficient anode material for lithium ion batteries. *J. Mat. Chem. A* 5 (10), 5007–5012. doi:10.1039/c6ta11058d

Gonçalves, J. M., da Silva, M. I., Toma, H. E., Angnes, L., Martins, P. R., and Araki, K. (2020). Trimetallic oxides/hydroxides as hybrid supercapacitor electrode materials: A review. *J. Mat. Chem. A* 8 (21), 10534–10570. doi:10.1039/d0ta02939d

Gong, Q., Li, Y., Huang, H., Zhang, J., Gao, T., and Zhou, G. (2018). Shape-controlled synthesis of Ni-CeO2@PANI nanocomposites and their synergetic effects on supercapacitors. *Chem. Eng. J.* 344, 290–298. doi:10.1016/j.cej.2018.03.079

Guan, B. Y., Kushima, A., Yu, L., Li, S., Li, J., and Lou, X. W. D. (2017). Coordination polymers derived general synthesis of multishelled mixed metal-oxide particles for hybrid supercapacitors. *Adv. Mat.* 29 (17), 1605902. doi:10.1002/adma.201605902

Huang, B., Pan, Z., Su, X., and An, L. (2018). Recycling of lithium-ion batteries: Recent advances and perspectives. *J. Power Sources* 399, 274–286. doi:10.1016/j.jpowsour.2018.07.116

Huang, G., Zhang, F., Du, X., Wang, J., Yin, D., and Wang, L. (2014). Core-shell NiFe2O4@TiO2 nanorods: An anode material with enhanced electrochemical performance for lithium-ion batteries. *Chem. Eur. J.* 20 (35), 11214–11219. doi:10.1002/chem.201403148

Islam, M., Ali, G., Jeong, M. G., Choi, W., Chung, K. Y., and Jung, H. G. (2017). Study on the electrochemical reaction mechanism of NiFe2O4 as a high-performance anode for Li-ion batteries. *ACS Appl. Mat. Interfaces* 9 (17), 14833–14843. doi:10.1021/acsami.7b01892

Jiang, Y., and Liu, J. (2019). Definitions of pseudocapacitive materials: A brief review. *Energy Environ. Mat.* 2 (1), 30–37. doi:10.1002/eem2.12028

Jiao, C., Wang, Z., Zhao, X., Wang, H., Wang, J., Yu, R., et al. (2019). Triple-shelled manganese-cobalt oxide hollow dodecahedra with highly enhanced performance for rechargeable alkaline batteries. *Angew. Chem. Int. Ed.* 58 (4), 996–1001. doi:10.1002/anie.201811683

Kang, S. H., Jo, Y. N., Prasanna, K., Santhoshkumar, P., Joe, Y. C., Vediappan, K., et al. (2019). Bandgap tuned and oxygen vacant TiO2−x anode materials with enhanced electrochemical properties for lithium ion batteries. *J. Ind. Eng. Chem.* 71, 177–183. doi:10.1016/j.jiec.2018.11.020

Li, J., Meng, Q., Zhang, Y., Peng, L., Yu, G., Marschilok, A. C., et al. (2019). Size-dependent kinetics during non-equilibrium lithiation of nano-sized zinc ferrite. *Nat. Commun.* 10 (1), 93. doi:10.1038/s41467-018-07831-5

Li, J., Wang, J., Liang, X., Zhang, Z., Liu, H., Qian, Y., et al. (2014). Hollow MnCo2O4 submicrospheres with multilevel interiors: From mesoporous spheres to yolk-in-double-shell structures. *ACS Appl. Mat. Interfaces* 6 (1), 24–30. doi:10.1021/am404841t

Li, L., Chen, W., Luo, W., Xiao, Z., Zhao, Y., Owusu, K. A., et al. (2019). Co0.5Ni0.5MoO4 double-shelled hollow spheres with enhanced electrochemical performance for supercapacitors and lithium-ion batteries. *Energy Technol.* 7 (8), 1801160. doi:10.1002/ente.201801160

Liang, J., Fan, Z., Chen, S., Ding, S., and Yang, G. (2014). Hierarchical NiCo2O4 nanosheets@halloysite nanotubes with ultrahigh capacitance and long cycle stability as electrochemical pseudocapacitor materials. *Chem. Mat.* 26 (15), 4354–4360. doi:10.1021/cm500786a

Liu, T., Gong, Q., Cao, P., Sun, X., Ren, J., Gu, S., et al. (2020). Preparations of NiFe2O4 yolk-shell@C nanospheres and their performances as anode materials for lithium-ion batteries. *Nanomaterials* 10 (10), 1994. doi:10.3390/nano10101994

Lu, Y., Nai, J., and Lou, X. W. (2018b). Formation of NiCo2V2O8 yolk–double shell spheres with enhanced lithium storage properties. *Angew. Chem. Int. Ed.* 130 (11), 2899–2903. doi:10.1002/anie.201800363

Lu, Y., Yu, L., Wu, M., Wang, Y., and Lou, X. W. D. (2018a). Construction of complex Co3O4 @Co3V2O8 hollow structures from metal-organic frameworks with enhanced lithium storage properties. *Adv. Mat.* 30 (1), 1702875. doi:10.1002/adma.201702875

Luo, L., Chen, Z., Ke, H., Sha, S., Cai, G., Li, D., et al. (2019). Facile synthesis of three-dimensional MgFe2O4/graphene aerogel composites for high lithium storage performance and its application in full cell. *Mat. Des.* 182, 108043. doi:10.1016/j.matdes.2019.108043

Luo, L., Cui, R., Liu, K., Qiao, H., and Wei, Q. (2014). Electrospun preparation and lithium storage properties of NiFe2O4 nanofibers. *Ionics* 21 (3), 687–694. doi:10.1007/s11581-014-1213-1

Mujahid, M., Ullah Khan, R., Mumtaz, M., Mubasher Soomro, S. A., and Ullah, S. (2019). $NiFe_2O_4$ nanoparticles/MWCNTs nanohybrid as anode material for lithium-ion battery. *Ceram. Int.* 45 (7), 8486–8493. doi:10.1016/j.ceramint.2019.01.160

Pramanik, S., Mondal, S., Mandal, A. C., Mukherjee, S., Das, S., Ghosh, T., et al. (2020). Role of oxygen vacancies on the green photoluminescence of microwave-assisted grown ZnO nanorods. *J. Alloys Compd.* 849, 156684. doi:10.1016/j.jallcom.2020.156684

Qu, L., Hou, X., Huang, X., Liang, Q., Ru, Q., Wu, B., et al. (2017). Self-assembled porous NiFe2O4 floral microspheres inlaid on ultrathin flake graphite as anode materials for lithium ion batteries. *ChemElectroChem* 4 (12), 3148–3155. doi:10.1002/celc.201700862

Ren, Y., Li, X., Wang, Y., Gong, Q., Gu, S., Gao, T., et al. (2022b). Self-template formation of porous yolk-shell structure Mo-doped NiCo2O4 toward enhanced lithium storage performance as anode material. *J. Mat. Sci. Technol.* 102, 186–194. doi:10.1016/j.jmst.2021.05.079

Ren, Y., Li, X., Wang, Y., Gu, S., Yang, C., Gao, T., et al. (2022a). Preparation of yolk–double shell Mn0.5Zn0.5Co2O4/C nanomaterials as anodes for high–performance lithium–ion batteries. *Appl. Mat. Today* 27, 101452. doi:10.1016/j.apmt.2022.101452

Shehnaz, Ullah, M., Ren, S., Hao, C., and Mustafa, G. (2021). Designing three-dimensional hierarchical porous chrysanthemum flower-like CoNiFe2O4/carbon spheres as high-performance electrode for supercapacitors and oxygen reduction reaction. *J. Mat. Sci. Mat. Electron.* 32 (15), 20306–20316. doi:10.1007/s10854-021-06536-8

Shen, H., Xia, X., Yan, S., Jiao, X., Sun, D., and Lei, W. (2021). SnO_2/$NiFe_2O_4$/graphene nanocomposites as anode materials for lithium ion batteries. *J. Alloy. Compd.* 853. doi:10.1016/j.jallcom.2020.157017

Shen, L., Yu, L., Yu, X. Y., Zhang, X., and Lou, X. W. (2015). Self-templated formation of uniform NiCo2O4 hollow spheres with complex interior structures for lithium-ion batteries and supercapacitors. *Angew. Chem. Int. Ed.* 54 (6), 1868–1872. doi:10.1002/anie.201409776

Song, W., Ji, K., Aguadero, A., Shearing, P. R., Brett, D. J. L., Xie, F., et al. (2018). Co3O4 hollow nanospheres doped with ZnCo2O4 via thermal vapor mechanism for fast lithium storage. *Energy Storage Mat.* 14, 324–334. doi:10.1016/j.ensm.2018.05.004

Tong, X., Zhao, L., Lin, X., Pan, X., Zhang, J., Duan, X., et al. (2017). High-index faceted nickel ferrite nanocrystals encapsulated by graphene with high performance for lithium-ion batteries. *Electrochim. Acta* 257, 99–108. doi:10.1016/j.electacta.2017.10.040

Wang, J., Fang, F., Yuan, T., Yang, J., Chen, L., Yao, C., et al. (2017). Three-dimensional graphene/single-walled carbon nanotube aerogel anchored with SnO2 nanoparticles for high performance lithium storage. *ACS Appl. Mat. Interfaces* 9 (4), 3544–3553. doi:10.1021/acsami.6b10807

Wang, J., Yang, G., Wang, L., and Yan, W. (2016). Synthesis of one-dimensional NiFe2O4 nanostructures: Tunable morphology and high-performance anode materials for Li ion batteries. *J. Mat. Chem. A Mat.* 4 (22), 8620–8629. doi:10.1039/c6ta02655a

Wang, J., Yang, N., Tang, H., Dong, Z., Jin, Q., Yang, M., et al. (2013). Accurate control of multishelled Co3O4 hollow microspheres as high-performance anode materials in lithium-ion batteries. *Angew. Chem. Int. Ed.* 52 (25), 6417–6420. doi:10.1002/anie.201301622

Wang, W., Zhao, Y., Zhang, Y., Wang, J., Cui, G., Li, M., et al. (2020). Defect-rich multishelled Fe-doped Co3O4 hollow microspheres with multiple spatial confinements to facilitate catalytic conversion of polysulfides for high-performance Li-S batteries. *ACS Appl. Mat. Interfaces* 12 (11), 12763–12773. doi:10.1021/acsami.9b21853

Wang, Z., Jia, W., Jiang, M., Chen, C., and Li, Y. (2016). One-step accurate synthesis of shell controllable CoFe2O4 hollow microspheres as high-performance

electrode materials in supercapacitor. *Nano Res.* 9 (7), 2026–2033. doi:10.1007/s12274-016-1093-y

Weng, C., Sun, X., Han, B., Ye, X., Zhong, Z., Li, W., et al. (2020). Targeted conversion of Ni in electroplating sludge to nickel ferrite nanomaterial with stable lithium storage performance. *J. Hazard. Mat.* 393, 122296. doi:10.1016/j.jhazmat.2020.122296

Wu, L. L., Wang, Z., Long, Y., Li, J., Liu, Y., Wang, Q. S., et al. (2017). Multishelled $Ni_x Co_{3-x} O_4$ hollow microspheres derived from bimetal-organic frameworks as anode materials for high-performance lithium-ion batteries. *Small* 13 (17), 1604270. doi:10.1002/smll.201604270

Wu, L., Sun, L., Li, X., Zhang, Q., Zhang, Y., Gu, J., et al. (2020). CuCo2S4 -rGO microflowers: First-principle calculation and application in energy storage. *Small* 16 (28), e2001468. doi:10.1002/smll.202001468

Xia, S. B., Huang, W. J., Shen, X., Liu, J., Cheng, F. X., Guo, H., et al. (2021). Fabrication of porous Ni/CoFe2O4@ C composite for pseudocapacitive lithium storage. *J. Alloys Compd.* 854, 157177. doi:10.1016/j.jallcom.2020.157177

Xiao, Y., Zai, J., Tian, B., and Qian, X. (2017). Formation of NiFe2O4/expanded graphite nanocomposites with superior lithium storage properties. *Nanomicro. Lett.* 9 (3), 34. doi:10.1007/s40820-017-0127-7

Xu, H., Zhao, L., Liu, X., Huang, Q., Wang, Y., Hou, C., et al. (2020). Metal-organic-framework derived core-shell N-doped carbon nanocages embedded with cobalt nanoparticles as high-performance anode materials for lithium-ion batteries. *Adv. Funct. Mat.* 30 (50), 2006188. doi:10.1002/adfm.202006188

Yang, T., Zhang, W., Li, L., Jin, B., Jin, E., Jeong, S., et al. (2017). *In-situ* synthesized ZnFe2O4 firmly anchored to the surface of MWCNTs as a long-life anode material with high lithium storage performance. *Appl. Surf. Sci.* 425, 978–987. doi:10.1016/j.apsusc.2017.07.152

Zhang, T., Zhang, L., Zhao, L., Huang, X., Li, W., Li, T., et al. (2020). Free-standing foldable V2O3/multichannel carbon nanofibers electrode for flexible Li-ion batteries with ultralong lifespan. *Small* 16 (47), 2005302. doi:10.1002/smll.202005302

Zhang, Y., Cao, W., Cai, Y., Shu, J., and Cao, M. (2019a). Rational design of NiFe2O4–rGO by tuning the compositional chemistry and its enhanced performance for a Li-ion battery anode. *Inorg. Chem. Front.* 6 (4), 961–968. doi:10.1039/c9qi00055k

Zhang, Y., Hu, K., Zhou, Y., Xia, Y., Yu, N., Wu, G., et al. (2019b). A facile one-step synthesis of silicon/silicon carbide/carbon nanotube nanocomposite as a cycling-stable anode for lithium ion batteries. *Nanomaterials* 9 (11), 1624. doi:10.3390/nano9111624

Zhou, P., Meng, H., Zhang, Z., Chen, C., Lu, Y., Cao, J., et al. (2017). Stable layered Ni-rich LiNi0.9Co0.07Al0.03O2 microspheres assembled with nanoparticles as high-performance cathode materials for lithium-ion batteries. *J. Mat. Chem. A* 5 (6), 2724–2731. doi:10.1039/C6TA09921A

Zou, Y., Li, Z., Liu, Y., Duan, J., and Long, B. (2020). Coaxial structure of NiFe2O4/CNTs composites as anodes for enhanced lithium ion batteries. *J. Alloys Compd.* 820, 153085. doi:10.1016/j.jallcom.2019.153085